RARE METALS

ORIGINAL ARTICLE

Freestanding carbon fiber-confined yolk-shelled silicon-based anode for promoted lithium storage applications

Dong-Chen Jia, Yuan-Yong Feng, Chuan-Long Zhang, Jian-Jiang Li, Bin-Wei Zhang, Yu-Hai Dou, Jagadish Chandra Roy*, Xiao-Yi Zhu*⬢ , Lei Zhang*⬢

Abstract A flexible carbon fiber-confined yolk-shelled silicon-based composite is reported as an anode material for lithium storage applications. Silicon nanoparticles (Si NPs) are confined by the N-doped hollow carbon cages (Si-NHC) and these uniform dispersed yolk-shell-structured Si-NHC units were encapsulated by the carbon fibers within an interconnected three-dimensional (3D) framework (Si-NHC@CNFs). For the encapsulated yolk-shelled Si-NHC, the void space between the inner Si NPs and outer NHC can accommodate the structural changes of Si NPs during charging/discharging processes, leading to effectively improved structural stability and cycling life. More importantly, all the Si-NHC units were bridged together through a conductive CNFs "highway" to enhance the overall conductivity and tap density further. As observed, Si-NHC@CNFs exhibited an initial discharge capacity of 1364.1 mAh·g^{-1} at 1000 mA·g^{-1} and 678.9 mAh·g^{-1} at 2000 mA·g^{-1}. Furthermore, the reversible capacity was well maintained at 752.2 mAh·g^{-1} at 500 mA·g^{-1} after 6000 ultra-long cycles.

Keywords Silicon; ZIF-8; Carbon fibers; Anode; Lithium-ion battery (LIB)

Dong-Chen Jia and Yuan-Yong Feng have contributed equally to this work.

D.-C. Jia, C.-L. Zhang, J.-J. Li, X.-Y. Zhu*
School of Environmental Science and Engineering, Qingdao University, Qingdao 266071, China
e-mail: xyzhu@qdu.edu.cn

Y.-Y. Feng
Department of Oral and Maxillofacial Surgery, The Affiliated Hospital of Qingdao University, Qingdao 266071, China

B.-W. Zhang
Center of Advanced Energy Technology and Electrochemistry, Institute of Advanced Interdisciplinary Studies, School of Chemistry and Chemical Engineering, Chongqing University, Chongqing 400044, China

Y.-H. Dou
Institute of Energy Materials Science, University of Shanghai for Science and Technology, Shanghai 200093, China

J. C. Roy*, L. Zhang*
Centre for Catalysis and Clean Energy, Gold Coast Campus, Griffith University, Southport, QLD 4222, Australia
e-mail: jagadish.roy@griffithuni.edu.au

L. Zhang
e-mail: lei.zhang@griffith.edu.au

1 Introduction

Silicon, considered the next generation of emerging high-specific-capacity anode materials, exhibits the advantages of excellent theoretical capacity ($\sim$ 4200 mAh·g^{-1}), environmental friendliness, natural abundance, and low charge/discharge potential [1]. However, in the discharge/charge (lithium/delithiation) process, the considerable volume change ($\sim$ 400%) [2] of Si-based anodes leads to serious comminution and the formation of an irreversible solid electrolyte interface (SEI) layer, which can instantly cause structural pulverization, thus reducing the electrochemical capacity and Coulomb efficiency [3–9].

Thereby, it is a superior approach to introduce silicon nanoparticles (Si NPs) into the carbon matrix to alleviate the critical volume expansion [10]. Zeolitic imidazolate

frameworks (ZIFs), a kind of unique metal–organic framework structure materials with imidazole or its derivatives as ligands, can form three-dimensional carbon nanocage frameworks due to the highly porous structure with sodalite topology [11–14]. Among various ZIFs, ZIF-8 is selected to fabricate carbon nanocages for silicon/carbon (Si/C) composites due to the high N-doped microporous nanostructure after high-temperature carbonization [15–17]. The pore size of ZIF-8 is known to be 0.34 nm, larger than that of a Li atom (0.30 nm) or Li-ion (0.15 nm) [18, 19], which is suitable for ions diffusion for high lithium storage. Additionally, the abundant nanopores and open channels of ZIF-8 provide a restrictive effect on the volume contraction and expansion of Si [20], further guaranteeing good structural integrity during cycling.

Li et al. [21] proposed an N-doped Si@NC structure through a straightforward and convenient preparation process using ZIF-8 serving as the carbon precursor. The composite exhibited improved lithium storage performance, i.e., the reversible capacity was 724 mAh·g^{-1} at 500 mA·g^{-1}, and remained 302 mAh·g^{-1} after 800 cycles. Xue et al. [22] developed a hollow nanocages Si structure (H-Si@C) by growing SiO_2 along the surface of ZIF-8 and converting it into Si via the magnesium thermal reduction process. The H-Si@C retained 1900 mAh·g^{-1} at 500 mA·g^{-1} after 200 cycles. Although ZIF-8 can present superior porous carbon nanocage frameworks to buffer Si volume expansion and improve cyclic stability [23–26], the nonconductive nature of the electrode still hinders their potential application [17]. Therefore, to further improve the overall conductivity of the electrode, a strategy is to bridge Si@C units through a conductive "highway" to enhance the transfer of Li ions and electrons during charging and discharging cycles [27, 28].

Electrospinning is an effective strategy to prepare conductive carbon fibers (CNFs) by electric field force [29]. CNFs prepared by electrospinning have interconnected 3D framework that can provide excellent mechanical properties and significant power transfer characteristics [30–32]. Meanwhile, CNFs develop a supporting framework for the structural changes in the process of lithium/delithiation, improve the electron transmission dynamics [33], and maximize the diffusion of Li ions in the pores [34].

Herein, a flexible carbon fiber-confined yolk-shelled Si/C structure was developed by encapsulating Si NPs in ZIF-8 carbon nanocages and further embedded in electrospinning CNFs frameworks (Scheme 1). First, SiO_2 derived from the hydrolysis of tetraethyl orthosilicate (TEOS) was coated on the surface of Si NPs (Si@SiO_2) to ensure good dispersion in the subsequent electrospinning process. Second, ZIF-8 was in situ synthesized, wrapping Si@SiO_2 NPs as a buffer framework (Si@SiO_2@ZIF-8). Then electrospinning was carried out, and polyacrylonitrile (PAN) was used as the spinning solution to obtain Si@SiO_2@ZIF-8@PAN. Finally, Si@SiO_2@ZIF-8@PAN was processed using the previously reported "pre-oxidation-slicing-carbonization" technique [35]. The final obtained sample Si@SiO_2@NC@CNFs, denoted as Si-NHC@CNFs, was directly used as an independent anode without adding any binder and collector. The collapse of organic ligands in the
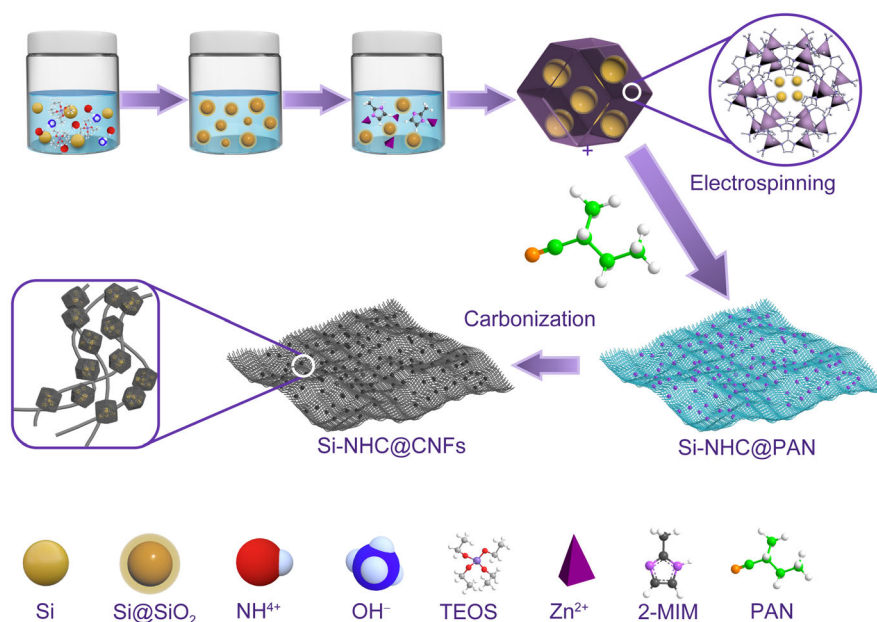
Scheme 1 Schematic illustration of Si-NHC@CNFs

ZIF-8 led to forming a porous carbon nanocage, which nicely wrapped Si@SiO₂ NPs to improve the mechanical strength and buffer volume expansion [36–38]. The derived porous polyhedra carbon nanocage was joined in series by interconnected electrospinning CNFs to form a flexible framework, enabling the rapid transmission of electrons and ions to reduce the resistance effectively to obtain excellent rate property and notable cycle performance.

2 Experimental

2.1 Materials

Analytical zinc nitrate hexahydrate ($Zn(NO_3)_2 \cdot 6H_2O$, > 99.0% Karat) was purchased from Guangrui Organism, and methanol (MeOH) and dimethylformamide (DMF) were bought from Sigma-Aldrich. In addition, 2-methylimidazole (2-MIM) was bought from MERYER, and PAN (molecular weight (M_w) = 150,000, Sinopharm) was bought from Shaoxing Gimel Advanced Materials Technology Co., Ltd. Si nanoparticles (~ 150 nm) were bought from JINLEI TECHNOLOGY. All chemicals purchased were not further treated after receipt.

2.2 Materials synthesis

2.2.1 Synthesis of Si@SiO₂@ZIF-8@PAN

Si@SiO₂ NPs were prepared by the well-established Stöber method. First, a certain amount of Si@SiO₂ NPs was dispersed in 100 ml MeOH and ultrasonic treated for 30 min to form Solution A. 6.16 g 2-MIM and 5.95 g $Zn(NO_3)_2 \cdot 6H_2O$ were dissolved in 100 ml MeOH to form Solutions B and C, respectively. Then, Solutions A and B were mixed and stirred for 30 min. Next, Si@SiO₂@ZIF-8 was prepared by adding solution C to the above-mixed solution and being stirred for 24 h, followed by centrifugation and washing. The Si@SiO₂@ZIF-8@PAN film was finally obtained after the electrospinning process using 9 g Si@SiO₂@ZIF-8 and 1 g PAN.

2.2.2 Synthesis of Si-NHC@CNFs

Si@SiO₂@ZIF-8@PAN film was processed using the previously reported "pre-oxidation-slicing-carbonization" method developed in our published work [35]. The obtained Si@SiO₂@NC@CNFs with various Si@SiO₂ contents were denoted as Si-NHC@CNFs#1 (250 mg), Si-NHC@CNFs#2 (300 mg), and Si-NHC@CNFs#3 (350 mg), respectively. For comparison, the sample named Si-NHC was prepared via the same synthetic process without electrospinning. NC@CNFs sample was synthesized by electrospinning pure ZIF-8 without adding Si@SiO₂ NPs.

2.3 Materials characterization

The crystalline structure was analyzed by X-ray diffractometer (XRD; Brooke XRD D8 VENTURE QUEST), and Raman spectroscopy characterized the carbon composition of the composite. The relative contents of various substances in the composite were obtained by a thermogravimetric analyzer (TGA; HITACHI, STA200). X-ray photoelectron spectroscopy (XPS; AXIS UltraDLD) was used to analyze the composition and valence of elements. The adsorption performance and pore size distribution were analyzed and detected by the Brunauer–Emmett–Teller (BET) testing instrument (CIQTEK, F-Sorb X400 CES). The surface morphology of the composite was observed by a scanning electron microscope (SEM; JEOL JSM-6390LV). The transmission electron microscope (TEM; JEOL Ltd.) was applied to characterize the morphologies of samples. The chemical constitution was analyzed by energy-dispersive spectroscopy (EDS). Finally, the spacing of light and dark stripes was measured by a high-resolution transmission electron microscope (HRTEM; HITACHI, Brooke XFlash6t30).

2.4 Electrochemical measurement

The Si-NHC@CNFs composites were cut into disks with a mass loading of 1.16 mg·cm⁻² and subsequently assembled as separate electrodes in a glove box for the CR2016 coin cell. The Si-NHC electrode was prepared by mixing Si-NHC powders, acetylene black, and polyvinylidene fluoride with a mass ratio of 7:2:1 and using non-methyl pyrrolidone as the solvent. The obtained slurry was coated on the copper foil and then cut into a disk to assemble the CR2016 coin cell in the glove box. The performance tests of all the assembled batteries were carried out by CT2001A battery tester in the voltage stage of 0−2 V. The electrochemical impedance was measured, and the cyclic voltammetry (CV) was performed by CHI-760 electrochemical workstation.

3 Results and discussion

Figure 1a demonstrates the XRD curves of Si-NHC@CNFs#1, Si-NHC@CNFs#2, and Si-NHC@CNFs#3. The diffraction peaks at 28.4°, 47.2°, and 56.2° are attributed to the (111), (220), and (311) planes of Si, respectively [39–41]. The broad peak at 25.0° is owing to the amorphous carbon generated by the pyrolysis of PAN and ZIF-8.
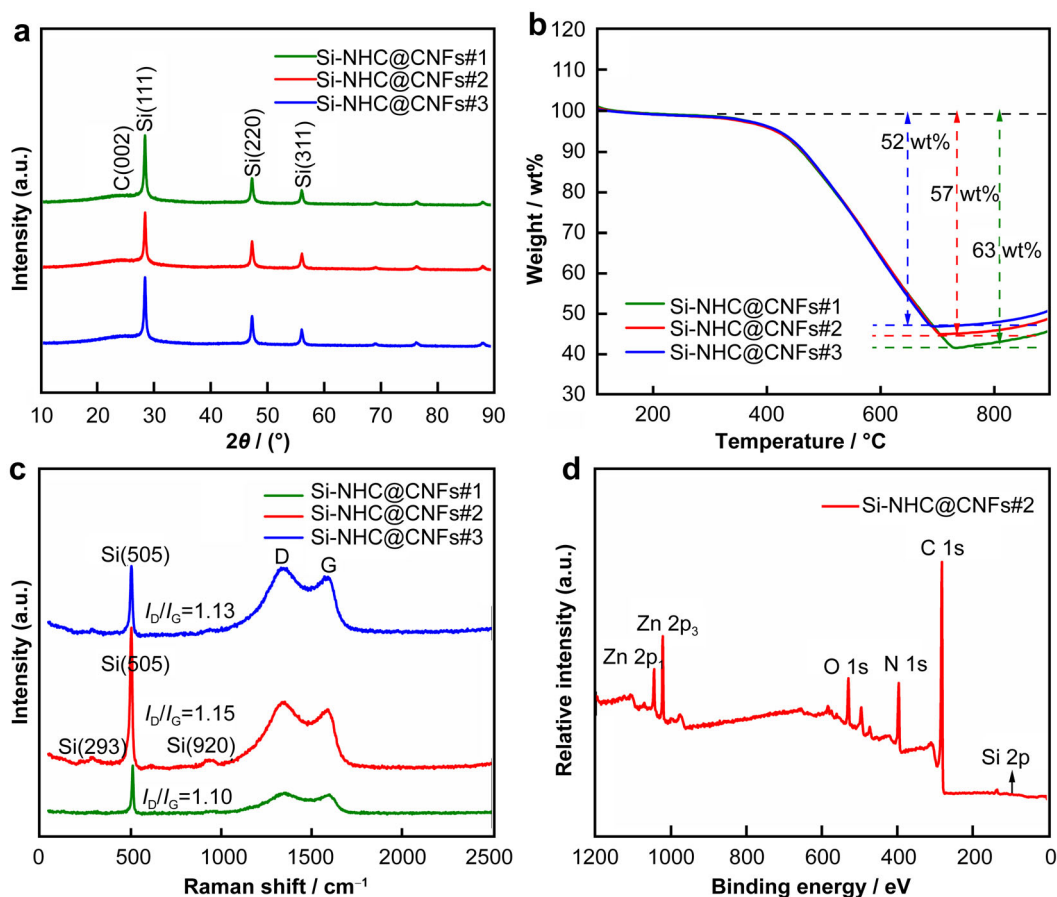
Fig. 1 **a** XRD patterns, **b** TGA curves, **c** Raman spectra of Si-NHC@CNFs (#1, #2, #3); **d** XPS spectrum of Si-NHC@CNFs#2

Figure 1b shows the TGA curves of Si-NHC@CNFs#1, Si-NHC@CNFs#2, and Si-NHC@CNFs#3. The weight loss started at 400 °C and ended at around 750 °C due to the carbon combustion in Si-NHC@CNFs. Thus, the carbon content in Si-NHC@CNFs (#1 to #3) can be roughly calculated to be around 63 wt%, 57 wt%, and 52 wt%, respectively. Figure S1 shows TGA curve of NC@CNFs, which was synthesized by electrospinning pure ZIF-8 without adding Si@SiO₂ NPs. Therefore, Si contents in Si-NHC@CNFs (#1 to #3) can be calculated to be around 25 wt%, 31 wt%, and 36 wt%, respectively. The curve increases slowly above 850 °C due to the slight oxidation of the Si and Zn in Si-NHC@CNFs.

Figure 1c shows the Raman spectra of Si-NHC@CNFs#1, Si-NHC@CNFs#2, and Si-NHC@CNFs#3. The peaks centered at 1360 and 1590 cm^{-1} represent disordered carbon (D band) and graphitic carbon (G band), respectively [11, 42]. The calculated totality ratios I_D/I_G are around 1.13, 1.15, and 1.10, respectively. It can be emphasized that the higher I_D/I_G value means more intercalation positions generation for Li-ions storage [7]. In addition, the absorption bands at 293,

505, and 920 cm^{-1} can be proved to be the peaks of crystalline Si.

XPS reflects the element composition, chemical state, and chemical bond information. Figure 1d shows the elemental composition of Si-NHC@CNFs#2, confirming the presence of Si, O, N, and C elements. The inconspicuous Si characteristic peak is due to the effective SiO₂ coating and double-walled NC and CNFs. Si 2p is divided into two peaks, 99.2 eV [1, 8] for Si–Si and 103.6 eV [4, 5] for Si–O in Fig. S2a. In addition, in the O 1s spectrum (Fig. S2b), the peak located at 533.6 eV is attributed to Si–O derived from the SiO₂ layer. Figure S2c indicates that the N 1s spectrum can be divided into three locations: graphitic-N (401.4 eV) [11, 13], pyrrolic-N (400 eV) [17, 19], and pyridinic-N (397.8 eV) [28, 29], respectively. In Fig. S2d, the C 1s spectrum can be divided into three peaks: C–C (284.6 eV), C–O (285.8 eV), and C=O (287.8 eV) [8–10]. The peaks located at 1021.1 and 1043 eV correspond to Zn 2p$_{3/2}$ and Zn 2p$_{1/2}$, respectively (Fig. S2e).

The N₂ adsorption–desorption properties of Si-NHC@CNFs are analyzed by BET measurement. Figure S3a shows the typical micropore absorption curves, and

the specific surface areas of Si-NHC@CNFs (#1 to #3) are 182.8, 226.8, and 167.0 $m^2 \cdot g^{-1}$ (Table S1). When the P/P_0 ratio (relative pressure) is 0.45–0.75, there is a hysteresis ring, indicating a mesoporous structure in the composite. ZIF-8-derived porous carbon nanocages and the interlinked CNFs developed by electrospinning contributed to the high surface area and porosity structure. Besides, the pore size distributions of Fig. S3b demonstrate the presence of micropores and mesopores (< 5 nm). More specifically, the higher surface area and preferred micropores and mesopores in Si-NHC@CNFs#2 can better facilitate electrolyte penetration and shorten Li-ions diffusion to promote rapid charge transfer during cycling. In addition, the typical porous microstructure can effectively accommodate Si volume expansion.

Figure 2 exhibits SEM images and corresponding enlarged view of Si-NHC@CNFs. Figure S4 shows the image of Si-NHC, which was synthesized by encapsulating Si@SiO$_2$ NPs into typical ZIF-8 carbon nanocages. Si-NHC exhibits uniform polyhedra morphology with a size of $\sim$ 1 μm, and Si@SiO$_2$ NPs can be completely wrapped by the carbon nanocages. After the electrospinning and carbonization process, Si-NHC nanocages are interlinked in series by CNFs ($\sim$ 250 nm) to form a 3D conductive framework. The dispersity of nanoparticle clusters along the CNFs, which may further affect the cycling performance, is greatly influenced by the concentration of the electrospinning solution [35]. Figure S5 shows EDS mapping images of Si-NHC@CNFs. It can be seen that the agglomeration phenomenon occurred with the increase in Si@SiO$_2$ contents. Figure 2a, b shows the overall morphology of Si-NHC@CNFs#1. A small number of particles are observed interlinked by CNFs. Figure 2c, d presents single and multiple fibers, demonstrating that polyhedral structures are individual, and a few are clustered together. NC@CNFs, fabricated by electrospinning pure ZIF-8 precursor without Si@SiO$_2$ content, display a similar cross-linked framework except for relatively smooth polyhedra (Fig. S6). With Si@SiO$_2$ NPs content increased to 300 mg, more polyhedral cages appeared and were sequentially interconnected by electrospun CNFs to form a uniform framework structure (Fig. 2e–g). As the Si@SiO$_2$ contents further increased to 350 mg (Fig. 2h–j), the interlinks of CNFs are interrupted by the aggregated bulk particles. Therefore, it can be concluded that the composite with optimum Si@SiO$_2$ contents and a uniform interlinked conductive framework are preferred for high specific capacity and good stability.

Figure 3 reveals TEM and HRTEM images of Si@SiO$_2$, Si-NHC, and Si-NHC@CNFs#2. Figure 3a reveals that Si NPs are coated by a SiO$_2$ layer and the size is $\sim$ 200 nm. EDS mapping images in Fig. S7 further demonstrate SiO$_2$
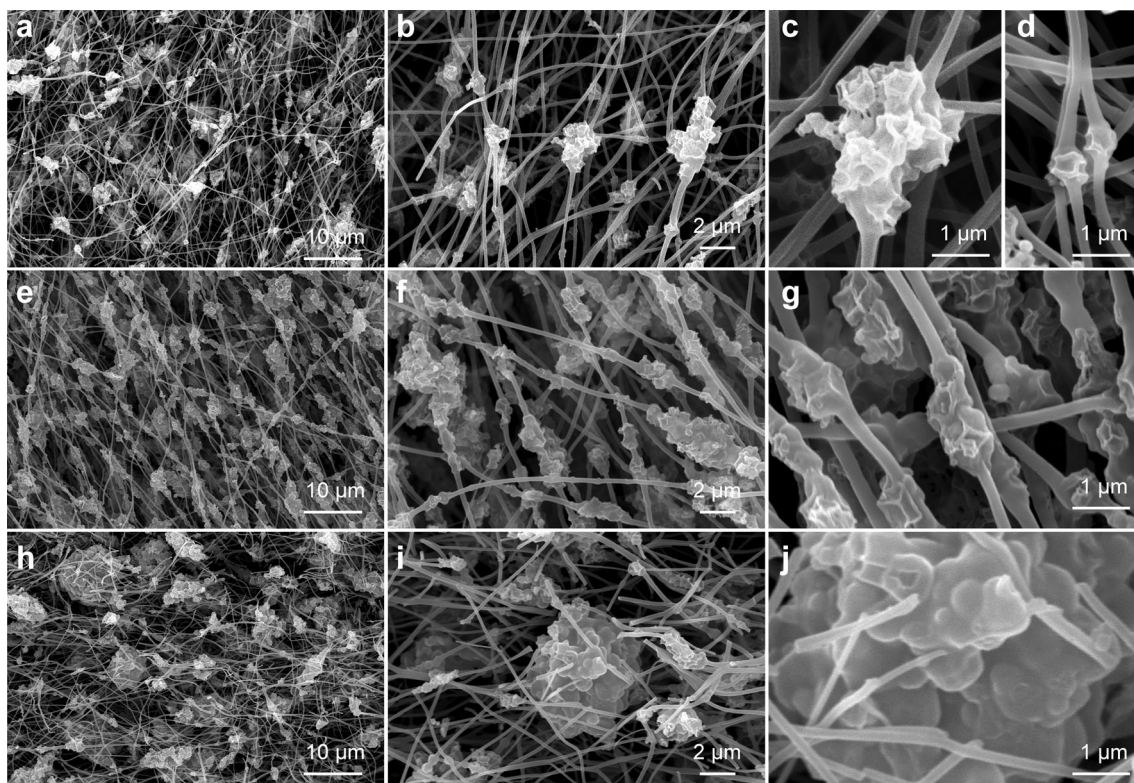

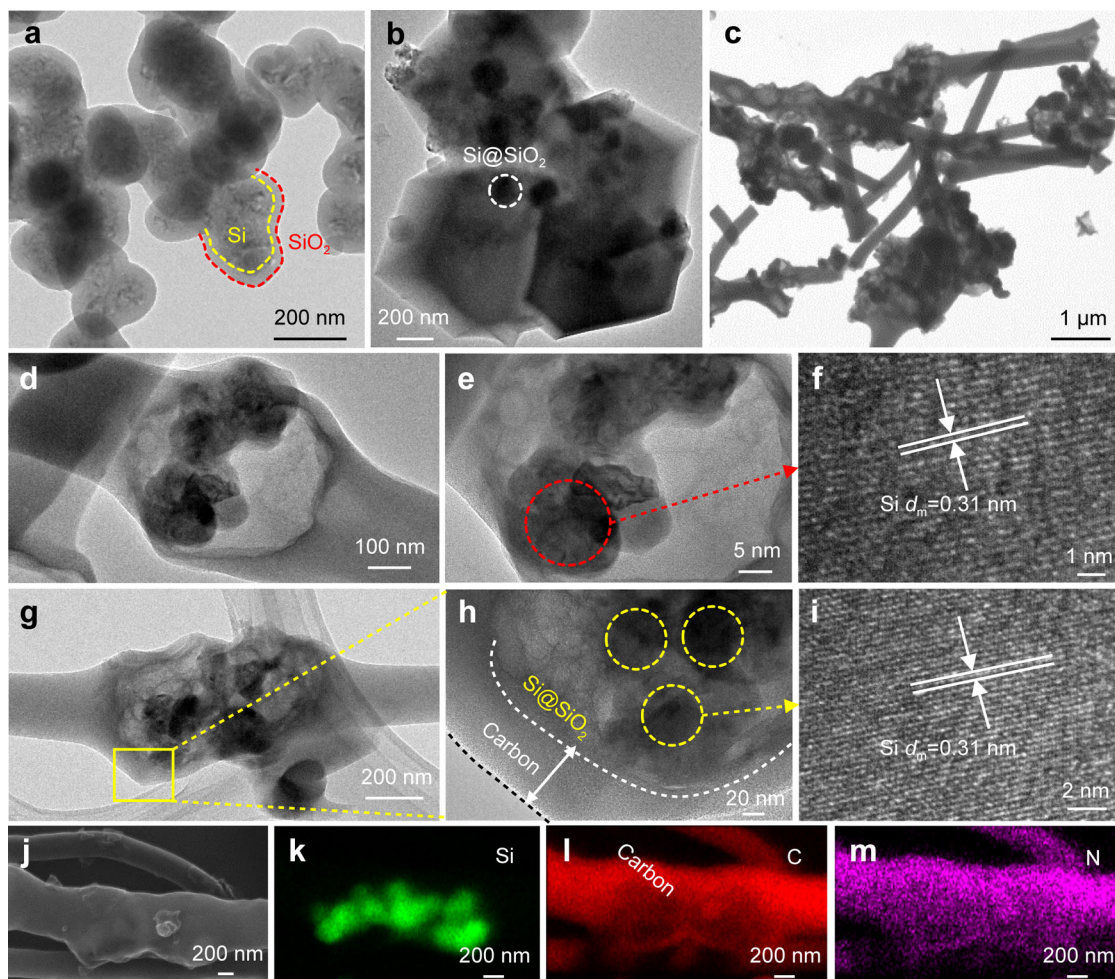**Fig. 2** SEM images of **a–d** Si-NHC@CNFs#1, **e–g** Si-NHC@CNFs#2, and **h–j** Si-NHC@CNFs#3

Fig. 3 TEM images of **a** Si@SiO$_2$, **b** Si@SiO$_2$@NHC, **c** Si-NHC@CNFs#2, **d, g** a single fiber, **e, h** corresponding enlarge view, **f, i** HRTEM image and **j–m** elemental mappings of Si-NHC@CNFs#2

coating. Figure 3b shows that Si@SiO$_2$@NC displays a typical dodecahedron structure (carbon nanocages), well-wrapped Si@SiO$_2$ NPs. The subsequent electrospinning process enables these carbon nanocages to be interconnected by crosslinked CNFs (Fig. 3c). Figure 3d, g reveals that Si@SiO$_2$ NPs are confined in carbon nanocages to form a typical yolk-shell structure. The TEM image of NC@CNFs in Fig. S8 confirms the similar hollow porous polyhedra microstructure derived from ZIF-8. Based on the structure analysis, it can be concluded that the void between particles and carbon shells can provide enough buffer space for volume expansion during cycling. Through the construction of a conductive 3D CNFs framework, rapid Li-ions transfer and enhanced overall electroconductivity can achieve the expected excellent rate capability. Figure 3f, i further illustrates the d-spacing of 0.31 nm, which corresponds to the (111) lattice plane of Si. The element distribution is measured by EDS mapping (Fig. 3j–m). It can be seen that elements C, N, Si, and Zn (Fig. S9) are regularly distributed along the CNFs. The

element distribution further confirms the typical yolk-shell structure, i.e., Si is located in the core while C forms the shell of the nanocage. In particular, the presence of Zn has been identified as a key feature that facilitates the formation of suitable porous structures to effectively accommodate Si volume expansion and the N derived from ZIF-8 increases active sites for the Li-ions storage [43].

Figure 4a shows CV profiles of Si-NHC@CNFs#2. In the primary discharge cycle, a broad peak located at 0.3 to 0.8 V can be attributed to the formation of the SEI layer and disappeared in the following cycles [40]. The peak at 0.18 V is due to the lithium process of Si. The peaks of 0.34 and 0.55 V are due to the conversion of Li$_x$Si to Si [44]. No significant peak displacement is observed in the subsequent two cycles, indicating good cycle stability.

The initial discharge and charge curves of the Si-NHC@CNFs#1, #2, #3, and Si-NHC at a current density of 1000 mA·g^{-1} are shown in Fig. 4b. During the first cycle, the platform of 0.3 to 0.8 V belongs to the formation of the SEI layer and the lithium reaction of Li$_x$Si, which
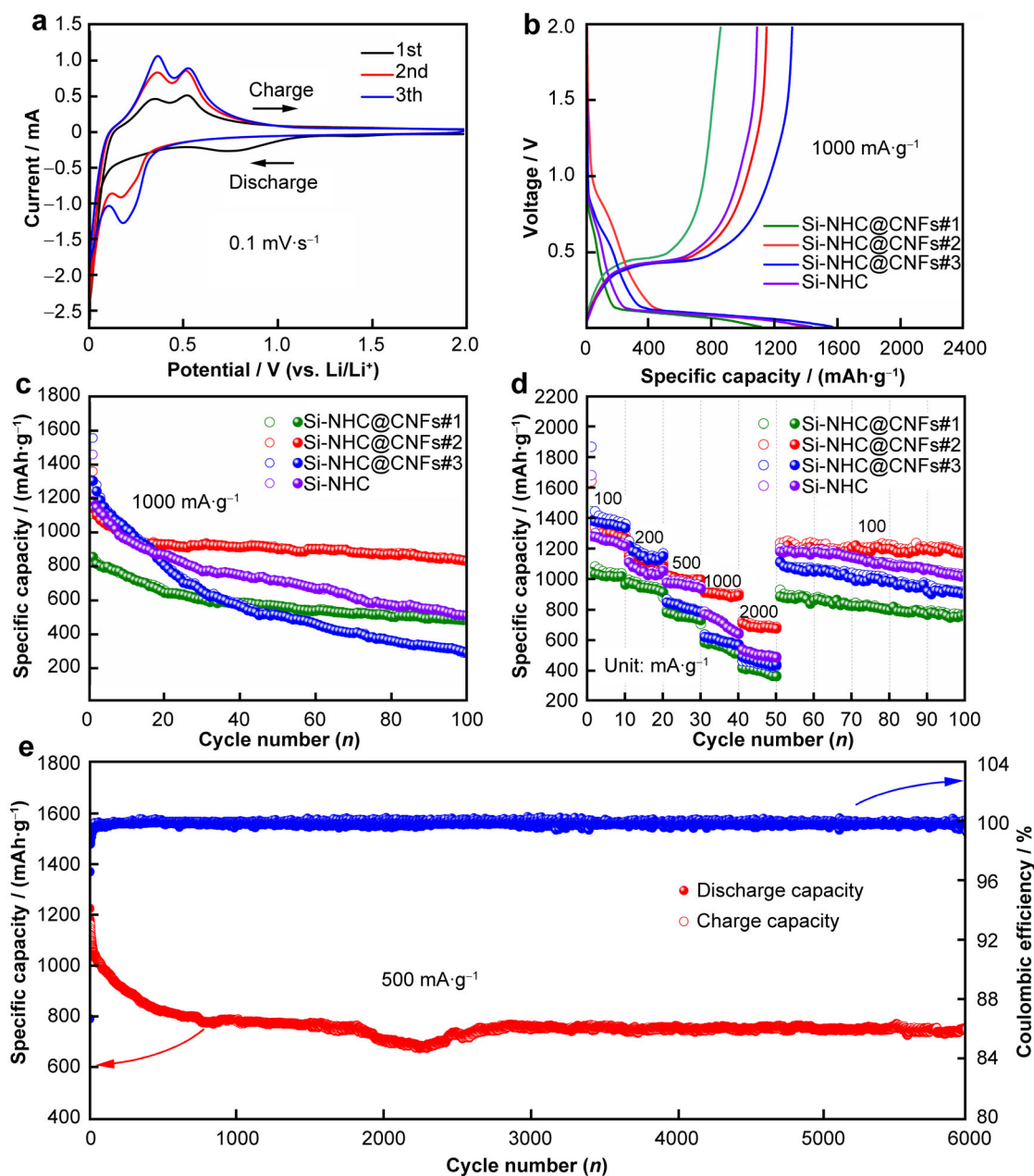
Fig. 4 Electrochemical performance: **a** CV diagram for the initial three cycles of Si-NHC@CNFs#2; **b** initial discharge and charge curves and **c** cycling performance of Si-NHC@CNFs#1, #2, #3, and Si-NHC at 1000 mA·g^{-1}; **d** rate properties of Si-NHC@CNFs#1, #2, #3, and Si-NHC; **e** ultra-long cycling stability of Si-NHC@CNFs#2 at 500 mA·g^{-1}

corresponds to the CV in Fig. 4a [41, 42, 45]. The first discharge and charge capacities for Si-NHC@CNFs#1, #2, #3, and Si-NHC are 1111.4 and 855.4 mAh·g^{-1}, 1364.1 and 1144.6 mAh·g^{-1}, 1562.2 and 1308.3 mAh·g^{-1}, 1463.5 and 1185.6 mAh·g^{-1}, and with corresponding initial Coulombic efficiencies (ICEs) of 76.96%, 83.90%, 83.74%, and 81.01%, respectively. The irreversible specific capacities are mainly due to the formation of SEI films.

Figure 4c shows the cycling performance of Si-NHC@CNFs and Si-NHC at 1000 mA·g^{-1}. The charge

capacities for Si-NHC@CNFs#1, #2, #3, and Si-NHC are 855.4, 1144.6, 1308.3, and 1185.6 mAh·g^{-1}, and after 100 cycles, the reversible capacities are 480.3, 830.6, 288.4, and 507.6 mAh·g^{-1}, respectively. Obviously, Si-NHC@CNFs#2 exhibits the best capacity retention of 72.57% after 100 cycles, indicating an optimum Si content in Si-NHC@CNFs. The low cyclic stability of Si-NHC may be attributed to the inadequate buffer of the microstructure, which is challenging to maintain the electrode integrity. The cycling performance of Si-
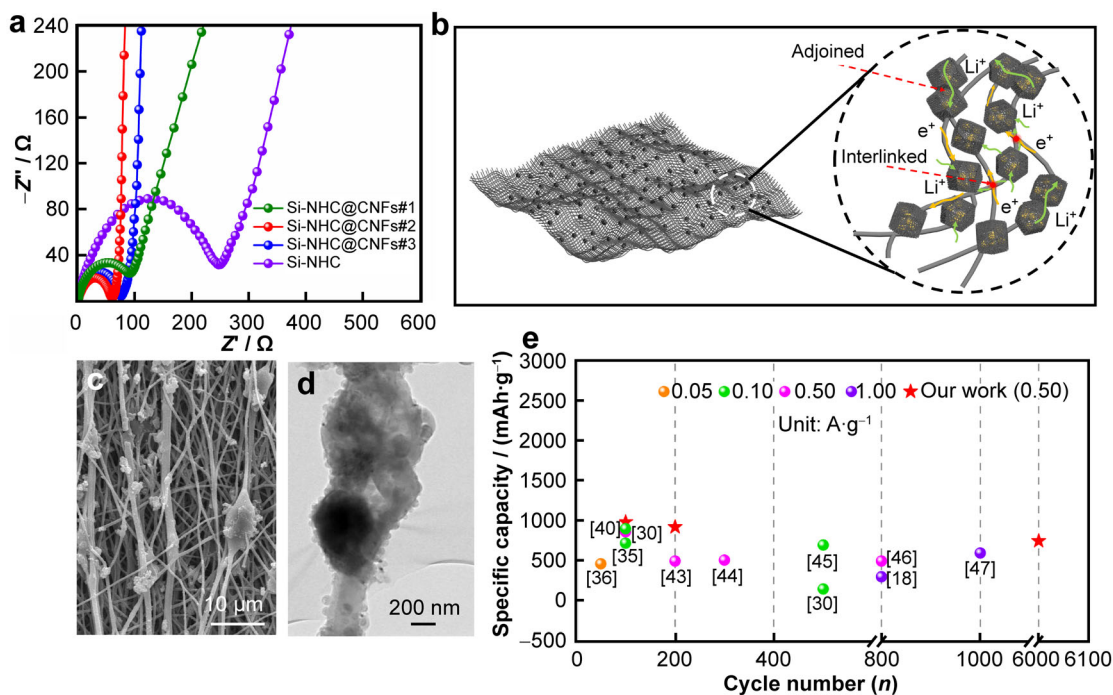
Fig. 5 **a** Electrochemical impedance spectra (EIS); **b** schematic illustration of ions migration for Si-NHC@CNFs; **c, d** SEM and TEM images of Si-NHC@CNFs#2 after 6000 cycles; **e** comparison of various kinds of Si/C anodes

NHC@CNFs#2 at 100 mA·g^{-1} is shown in Fig. S10. The specific capacity reaches 1105.9 mAh·g^{-1} at 100 mA·g^{-1} after 200 cycles.

Figure 4d shows the rate properties of Si-NHC@CNFs#1, #2, #3, and Si-NHC at different current densities. As anticipated, Si-NHC@CNFs#2 represented relatively excellent capacity properties at higher current densities. The reversible charging capacity of Si-NHC@CNFs#2 is 678.9 mAh·g^{-1} at 2000 mA·g^{-1} and retains 95.38% after 10 cycles. When the current density is restored to 100 mA·g^{-1}, the capacity recovers 92.3% of the initial capacity. The excellent rate performance is attributed to the flexible conductive framework given by electrospinning and the rich N content derived from ZIF-8, both of which can realize rapid Li-ions insertion and extraction.

Figure 4e shows the long-term cycling performance of Si-NHC@CNFs#2 at 500 mA·g^{-1}. The initial discharge and charge capacities of the anode are 1224.5 and 1061.7 mAh·g^{-1}, with an ICE of 86.71%. After 6000 cycles, the reversible specific capacity is well maintained at 752.2 mAh·g^{-1}, and the CE archives 99.27%. The obvious loss of initial capacity is due to the formation of the SEI film of Si. The electronic photograph and SEM images of Si-NHC@CNFs#2 after 6000 cycles are illustrated in Fig. S11. After cycling, Si-NHC NPs and CNFs are somewhat expanded, but the structure still can be maintained. Figure S12 shows that the reversible capacity of the

Si-NHC is only 699.3 mAh·g^{-1} at 100 mA·g^{-1} after 100 cycles. The rapid cycle decay of Si-NHC indicates that a porous dodecahedral carbon nanocage derived from ZIF-8 only partially alleviates the volume expansion of Si, and a more effective buffer layer is needed to ensure structural integrity.

Figure 5a shows the Nyquist plots of Si-NHC@CNFs, which are measured to investigate the kinetics. The semicircular for Si-NHC@CNFs#2 is much smaller than those of other samples, indicating the minimum resistance and the fastest electron transfer, which is attributed to the superior microstructure of flexible conductive framework and thus acquires notable rate properties [46]. Figure 5b shows the diffusion and migration mechanism of Li ions and electrons. Si-NHC@CNFs composite provides a superior structure to realize the higher specific capacity, excellent rate property, and honor cycling stability [47, 48]. Si@SiO$_2$ NPs which provide high specific capacity are successfully confined by porous carbon nanocages derived from ZIF-8 to form a yolk-shell structure to effectively alleviate the volume change during cycling [49, 50]. The electrospun CNFs interconnected these carbon nanocages to construct a flexible framework (Fig. S13), providing conductive "highway" channels to enable fast electron transfer for excellent rate performance. Even after ultrahigh 6000 cycles, this CNF-confined yolk-shell structure can maintain a relatively intact structural morphology (Fig. 5c, d). Figure 5e compares Si-NHC@CNFs with

other Si/C anodes reported in previous works. Obviously, Si-NHC@CNFs display superior ultra-long cycle stability with competitive specific capacity. As we know, in-depth studies on the ultra-long performance of Si/C anodes are rarely reported. Si-NHC@CNFs investigated in this work exhibit supreme cycling performance and are a typical representative of freestanding electrodes for high-energy–density lithium storage applications.

4 Conclusion

In summary, a freestanding carbon fiber-confined yolk-shelled silicon-based anode was prepared by encapsulating Si NPs in ZIF-8-derived carbon nanocages and subsequently interlinked by electrospun CNFs. N-doped carbon nanocage derived from ZIF-8 realized yolk-shelled structure to alleviate volume change of Si. CNFs interconnected these carbon cages in one system to improve the electroconductivity and cyclic stability. This superior structure gives full play to the conductivity of CNFs, and the advantage of porous N-doped carbon nanocages. Therefore, Si-NHC@CNFs with optimum Si contents exhibit the supreme ultra-long cycle performance, with a reversible capacity of 752.2 mAh·g^{-1} after 6000 cycles. Thus, this freestanding silicon-based composite structure has unlimited potential and is expected to become a new generation of anodes for high-energy-density lithium storage devices.

Declarations

References

[1] Zhang L, Huang QW, Liao XZ, Dou YH, Liu PR, Al-Mamun M, Wang Y, Zhang SQ, Zhao SL, Wang D, Meng GW, Zhao HJ. Scalable and controllable fabrication of CNTs improved yolk-shelled Si anodes with advanced in operando mechanical quantification. Energy Environ Sci. 2021;14(6):3502. https://doi.org/10.1039/D1EE00639H.

[2] Zhou XM, Liu Y, Du CY, Ren Y, Xiao R, Zuo PJ, Yin GP, Ma YL, Cheng XQ, Gao YZ. Layer-by-layer engineered silicon-based sandwich nanomat as flexible anode for lithium-ion batteries. ACS Appl Mater Interfaces. 2019;11(43):39970. https://doi.org/10.1021/acsami.9b13353.

[3] Bezza I, Trouillet V, Fiedler A, Bruns M, Indris S, Ehrenberg H, Saadoune I. Understanding the lithiation/delithiation process in SnP$_2$O$_7$ anode material for lithium-ion batteries. Electrochim Acta. 2017. https://doi.org/10.1016/j.electacta.2017.09.023.

[4] McDowell MT, Lee SW, Harris JT, Korgel BA, Wang C, Nix WD, Cui Y. In situ TEM of two-phase lithiation of amorphous silicon nanospheres. Nano Lett. 2013;13(2):758. https://doi.org/10.1021/nl3044508.

[5] Magasinski A, Dixon P, Hertzberg B, Kvit A, Ayala J, Yushin G. High-performance lithium-ion anodes using a hierarchical bottom-up approach. Nat Mater. 2010;9(4):353. https://doi.org/10.1038/nmat2725.

[6] Luo W, Wang YX, Wang LJ, Jiang W, Chou SL, Dou SX, Liu HK, Yang JP. Silicon/mesoporous carbon/crystalline TiO$_2$ nanoparticles for highly stable lithium storage. ACS Nano. 2016;10(11):10524. https://doi.org/10.1021/acsnano.6b06517.

[7] Luo W, Shen DK, Zhang RY, Zhang BW, Wang YX, Dou SX, Liu HK, Yang JP. Germanium nanograin decoration on carbon shell: boosting lithium-storage properties of silicon nanoparticles. Adv Funct Mater. 2016;26(43):7800. https://doi.org/10.1002/adfm.201603335.

[8] Mei SX, Guo SG, Xiang B, Deng JG, Fu JJ, Zhang XM, Zheng Y, Gao B, Chu PK, Kf H. Enhanced ion conductivity and electrode–electrolyte interphase stability of porous Si anodes enabled by silicon nitride nanocoating for high-performance Li-ion batteries. J Energy Chem. 2022. https://doi.org/10.1016/j.jechem.2022.02.002.

[9] Yan YT, Zhao XL, Dou HL, Wei JJ, Zhao WY, Sun ZH, Yang XW. Rational design of robust nano-Si/graphite nanocomposites anodes with strong interfacial adhesion for high-performance lithium-ion batteries. Chin Chem Lett. 2021;32(2):910. https://doi.org/10.1016/j.cclet.2020.07.021.

[10] Chen T, Wu J, Zhang QL, Su X. Recent advancement of SiO$_x$ based anodes for lithium-ion batteries. J Power Sources. 2017. https://doi.org/10.1016/j.jpowsour.2017.07.073.

[11] Samuel E, Park C, Kim T, Joshi B, Aldalbahi A, Alanzi HS, Swihart MT, Yoon WY, Yoon SS. Dodecahedral ZnO/C framework on reduced graphene oxide sheets for high-performance Li-ion battery anodes. J Alloys Compd. 2020. https://doi.org/10.1016/j.jallcom.2020.155208.

[12] Zhang YQ, Lu YB, Feng S, Liu DD, Ma ZL, Wang SY. On-site evolution of ultrafine ZnO nanoparticles from hollow metal–organic frameworks for advanced lithium ion battery anodes. J Mater Chem A. 2017;5(43):22512. https://doi.org/10.1039/C7TA08284C.

[13] Yuan G, Cao R, Geng M, Jin HF, Li B, Xu Q. Zeolitic imidazolate frameworks-derived activated carbon as electrode material for lithium-sulfur batteries and lithium-ion batteries. J Electron Mater. 2020;49(10):6156. https://doi.org/10.1007/s11664-020-08378-2.

[14] Xu XL, Wang H, Xie YZ, Liu JB, Yan H, Liu W. Graphitized mesoporous carbon derived from ZIF-8 for suppressing sulfation in lead acid battery and dendritic lithium formation in lithium ion battery. J Electrochem Soc. 2018;165(13):A2978. https://doi.org/10.1149/2.0361813jes.

[15] Qian XY, Jin LN, Wang SW, Yao SS, Rao DW, Shen XQ, Xi XM, Xiang J. Zn-MOF derived micro/meso porous carbon nanorod for high performance lithium–sulfur battery. RSC Adv. 2016;6(97):94629. https://doi.org/10.1039/C6RA19356K.

[16] Zhang H, Wang YS, Zhao WQ, Zou MC, Chen YJ, Yang LS, Xu L, Wu HS, Cao AY. MOF-derived ZnO zanoparticles covered by N-doped carbon layers and hybridized on carbon nanotubes for lithium-ion battery anodes. ACS Appl Mater Interfaces. 2017;9(43):37813. https://doi.org/10.1021/acsami.7b12095.

[17] Ye MH, Li CX, Zhao Y, Qu LT. Graphene decorated with bimodal size of carbon polyhedrons for enhanced lithium storage. Carbon. 2016. https://doi.org/10.1016/j.carbon.2016.05.013.

[18] Zhou YT, Huang QY, Low CTJ, Walton RI, McNally T, Wan CY. Heteroatom-doped core/shell carbonaceous framework materials: synthesis, characterization and electrochemical properties. New J Chem. 2019;43(14):5632. https://doi.org/10.1039/C8NJ05193C.

[19] Yu YJ, Yue C, Lin XG, Sun SB, Gu JP, He X, Zhang CH, Lin W, Lin DH, Liao XL, Xu BB, Wu ST, Zheng MS, Li J, Kang JY, Lin LW. ZIF-8 cooperating in TiN/Ti/Si nanorods as efficient anodes in micro-lithium-ion-batteries. ACS Appl Mater Interfaces. 2016;8(6):3992. https://doi.org/10.1021/acsami.5b11287.

[20] Li Q, Zhang H, Lou SF, Qu YT, Zuo PJ, Ma YL, Cheng XQ, Du CY, Gao YZ, Yin GP. Pseudocapacitive Li+ intercalation in ZnO/ZnO@C composites enables high-rate lithium-ion storage and stable cyclability. Ceram Int. 2017;43(15):11998. https://doi.org/10.1016/j.ceramint.2017.06.051.

[21] Li QG, Wang YH, Gao XY, Li HF, Tan QQ, Zhong ZY, Su FB. Enhancement of ZIF-8 derived N-doped carbon/silicon composites for anode in lithium ions batteries. J Alloys Compd. 2021. https://doi.org/10.1016/j.jallcom.2021.159712.

[22] Xue HJ, Wu YQ, Wang ZM, Shen YB, Sun QJ, Liu G, Yin DM, Wang LM, Li Q, Ming J. Unraveling the new role of metal-organic frameworks in designing silicon hollow nanocages for high-energy lithium-ion batteries. ACS Appl Mater Interfaces. 2021;13(34):40471. https://doi.org/10.1021/acsami.1c07495.

[23] Huang G, Zhang FF, Du XC, Qin YL, Yin DM, Wang LM. Metal organic frameworks route to in situ insertion of multi-walled carbon nanotubes in Co3O4 polyhedra as anode materials for lithium-ion batteries. ACS Nano. 2015;9(2):1592. https://doi.org/10.1021/nn506252u.

[24] Zhong HX, Wang J, Zhang YW, Xu WL, Xing W, Xu D, Zhang YF, Zhang XB. ZIF-8 derived graphene-based nitrogen-doped porous carbon sheets as highly efficient and durable oxygen reduction electrocatalysts. Angew Chem Int Ed. 2014;53(51):14235. https://doi.org/10.1002/anie.201408990.

[25] Sun CC, Yang J, Rui XH, Zhang WN, Yan QY, Chen P, Huo FW, Huang W, Dong XC. MOF-directed templating synthesis of a porous multicomponent dodecahedron with hollow interiors for enhanced lithium-ion battery anodes. J Mater Chem A. 2015;3(16):8483. https://doi.org/10.1039/C5TA00455A.

[26] Zhao XJ, Jia W, Wu XY, Lv Y, Qiu JS, Guo JX, Wang XC, Jia DZ, Yan JF, Wu DL. Ultrafine MoO3 anchored in coal-based carbon nanofibers as anode for advanced lithium-ion batteries. Carbon. 2020. https://doi.org/10.1016/j.carbon.2019.09.065.

[27] Samuel E, Joshi B, Kim MW, Kim Y, Park S, Kim TG, Swihart MT, Yoon WY, Yoon SS. Zeolitic imidazolate framework-8 derived zinc oxide/carbon nanofiber as freestanding electrodes for lithium storage in lithium-ion batteries. J Power Sources. 2018. https://doi.org/10.1016/j.jpowsour.2018.05.068.

[28] Xu XL, Wang H, Liu JB, Yan H. The applications of zeolitic imidazolate framework-8 in electrical energy storage devices: a review. J Mater Sci Mater Electron. 2017;28(11):7532. https://doi.org/10.1007/s10854-017-6485-6.

[29] Jin T, Han QQ, Wang YJ, Jiao LF. 1D nanomaterials: design, synthesis, and applications in sodium–ion batteries. Small. 2018;14(2):1703086. https://doi.org/10.1002/smll.201703086.

[30] Cong LN, Xie HM, Li JH. Hierarchical structures based on two-dimensional nanomaterials for rechargeable lithium batteries. Adv Energy Mater. 2017;7(12):1601906. https://doi.org/10.1002/aenm.201601906.

[31] McCann JT, Li D, Xia YN. Electrospinning of nanofibers with core-sheath, hollow, or porous structures. J Mater Chem. 2005;15(7):735. https://doi.org/10.1039/B415094E.

[32] Li D, Xia Y. Electrospinning of nanofibers: reinventing the wheel. Adv Mater. 2004;16(14):1151. https://doi.org/10.1002/adma.200400719.

[33] Inagaki M, Yang Y, Kang FY. Carbon nanofibers prepared via electrospinning. Adv Mater. 2012;24(19):2547. https://doi.org/10.1002/adma.201104940.

[34] Wang HK, Wu QZ, Cao DX, Lu X, Wang JK, Leung MKH, Cheng SD, Lu L, Niu CM. Synthesis of SnSb-embedded carbon-silica fibers via electrospinning: effect of TEOS on structural evolutions and electrochemical properties. Mater Today Energy. 2016;1–2(1):24. https://doi.org/10.1016/j.mtener.2016.11.003.

[35] Li XH, Wang XX, Li JJ, Liu G, Jia DC, Ma ZL, Zhang L, Peng Z, Zhu XY. High-performance, flexible, binder-free silicon–carbon anode for lithium storage applications. Electrochem Commun. 2022. https://doi.org/10.1016/j.elecom.2022.107257.

[36] Lee YW, Kim DM, Kim SJ, Kim MC, Choe HS, Lee KH, Sohn JI, Cha SN, Kim JM, Park KW. In situ synthesis and characterization of Ge embedded electrospun carbon nanostructures as high performance anode material for lithium-ion batteries. ACS Appl Mater Interfaces. 2016;8(11):7022. https://doi.org/10.1021/acsami.5b12284.

[37] Jiang YQ, Li CH, Yu RH, Wang YT, Zhou L. Realizing Sub-5 nm red phosphorus dispersion in a SiOx/C matrix for enhanced lithium storage. ACS Appl Mater Interfaces. 2022;14(23):26775. https://doi.org/10.1021/acsami.2c05293.

[38] Wang F, Liao XB, Wang HY, Zhao Y, Mao J, Truhlar DG. Bioinspired mechanically interlocking holey graphene@SiO2 anode. Interdiscip Mater. 2022;1(4):517. https://doi.org/10.1002/idm2.12032.

[39] Zhang YT, Zhang KB, Jia KL, Liu GY, Zhang YL, Liu W, Li KK, Zhang BC, Wang P. Facile synthesis 2D hierarchical structure of ultrahigh nitrogen-doped porous carbon graphene nanosheets as high-efficiency lithium-ion battery anodes. Mater Chem Phys. 2020. https://doi.org/10.1016/j.matchemphys.2020.123043.

[40] Zhang FZ, Ma YY, Jiang MM, Luo W, Yang JP. Boron heteroatom-doped silicon–carbon peanut-like composites enables long life lithium-ion batteries. Rare Met. 2022;41(4):1276. https://doi.org/10.1007/s12598-021-01741-0.

[41] Zhu GJ, Guo R, Luo W, Liu HK, Jiang W, Dou SX, Yang JP. Boron doping-induced interconnected assembly approach for mesoporous silicon oxycarbide architecture. Natl Sci Rev. 2021;8(6):nwaa152. https://doi.org/10.1093/nsr/nwaa152.

[42] Guan P, Li JJ, Lu TG, Guan T, Ma ZL, Peng Z, Zhu XY, Zhang L. Facile and scalable approach to fabricate granadilla-like porous-structured silicon-based anode for lithium ion batteries. ACS Appl Mater Interfaces. 2018;10(40):34283. https://doi.org/10.1021/acsami.8b12071.

[43] Liu HD, Li ZY, Zhang L, Ruan HB, Hu R. MOF-derived ZnSe/ N-doped carbon composites for lithium-ion batteries with enhanced capacity and cycling life. Nanoscale Res Lett. 2019; 14(1):237. https://doi.org/10.1186/s11671-019-3055-2.

[44] Liu G, Zhu XY, Li XH, Jia DC, Li D, Ma ZL, Li JJ. Flexible porous silicon/carbon fiber anode for high-performance lithium-ion batteries. Materials. 2022;15(9):3190. https://doi.org/10. 3390/ma15093190.

[45] Dirican M, Yildiz O, Lu Y, Fang XM, Jiang H, Kizil H, Zhang XW. Flexible binder-free silicon/silica/carbon nanofiber composites as anode for lithium–ion batteries. Electrochim Acta. 2015. https://doi.org/10.1016/j.electacta.2015.04.035.

[46] Zhang J, Zuo SL, Wang YQ, Yin HH, Wang ZQ, Wang J. Scalable synthesis of interconnected hollow Si/C nanospheres enabled by carbon dioxide in magnesiothermic reduction for high-performance lithium energy storage. J Power Sources. 2021. https://doi.org/10.1016/j.jpowsour.2021.229803.

[47] Tian HJ, Tan XJ, Xin FX, Wang CS, Han WQ. Micro-sized nano-porous Si/C anodes for lithium ion batteries. Nano Energy. 2015. https://doi.org/10.1016/j.nanoen.2014.11.031.

[48] Qian LZ, Lan JL, Xue MY, Yu YH, Yang XP. Two-step ball-milling synthesis of a Si/SiO$_x$/C composite electrode for lithium ion batteries with excellent long-term cycling stability. RSC Adv. 2017;7(58):36697. https://doi.org/10.1039/C7RA06671F.

[49] Xiao W, Qiu YJ, Xu Q, Wang JJ, Xie C, Peng JH, Hu JH, Zhang JJ, Li XF. Building sandwich-like carbon coated Si@CNTs composites as high-performance anode materials for lithium-ion batteries. Electrochim Acta. 2020. https://doi.org/10.1016/j. electacta.2020.137278.

[50] Li YX, Liu L, Liu XY, Feng Y, Xue BC, Yu LY, Ma LJ, Zhu YC, Chao YM, Wang XF. Extracting lignin-SiO$_2$ composites from Si-rich biomass to prepare Si/C anode materials for lithium ions batteries. Mater Chem Phys. 2021. https://doi.org/10.1016/j. matchemphys.2021.124331.